International Journal of
Molecular Sciences

MDPI

Article

Catalytic Reaction Mechanism of NO–CO on the ZrO_2 (110) and (111) Surfaces

Xuesong Cao [1], Chenxi Zhang [2,*], Zehua Wang [1] and Xiaomin Sun [1,*]

[1] Environment Research Institute, Shandong University, Qingdao 266200, China; xuesongcao@mail.sdu.edu.cn (X.C.); sdzhw@mail.sdu.edu.cn (Z.W.)

[2] College of Biological and Environmental Engineering, Binzhou University, Binzhou 256600, China; sdzhangcx@gmail.com

* Correspondence: sdzhangcx@gmail.com (C.Z.); sxmwch@sdu.edu.cn (X.S.)

Received: 3 October 2019; Accepted: 3 December 2019; Published: 5 December 2019

Abstract: Due to the large population of vehicles, significant amounts of carbon monoxide (CO), nitrogen oxides (NO_x), and unburned hydrocarbons (HC) are emitted into the atmosphere, causing serious pollution to the environment. The use of catalysis prevents the exhaust from entering the atmosphere. To better understand the catalytic mechanism, it is necessary to establish a detailed chemical reaction mechanism. In this study, the adsorption behaviors of CO and NO, the reaction of NO reduction with CO on the ZrO_2 (110) and (111) surfaces was performed through periodic density functional theory (DFT) calculations. The detailed mechanism for CO_2 and N_2 formation mainly involved two intermediates N_2O complexes and NCO species. Moreover, the existence of oxygen vacancies was crucial for NO reduction reactions. From the calculated energy, it was found that the pathway involving NCO intermediate interaction occurring on the ZrO_2 (110) surface was most favorable. Gas phase N_2O formation and dissociation were also considered in this study. The results indicated the role of reaction intermediates NCO and N_2O in catalytic reactions, which could solve the key scientific problems and disputes existing in the current experiments.

Keywords: Nitric oxide; Carbon monoxide; Zirconium dioxide; Density functional theory; Reaction mechanism

1. Introduction

Heterogeneous catalysis always be used to decrease the emission of automobile exhausts (CO, NO_x and HC), such as the Rhodium catalytic system to convert toxic gas NO to inactive product N_2 [1,2]. However, the rare and expensive characteristics of noble metal Rh limit its widespread use. Thus, quantities of investigations have been conducted to develop effective and economical catalyst systems.

As zirconium dioxide (ZrO_2) has high thermal stability, excellent redox properties and an acid–basic site on its surface, it is a good catalyst and support material for various reactions, such as CO_2 methanation [3,4], water–gas shift [5,6], NH_3 selective catalytic reduction [7,8], and hydrodeoxygenation [9,10]. Especially, the transition metal oxide dispersed onto the surface of ZrO_2 exhibits powerful activity for NO reduction. Okamoto et al. [11] found that Cu/ZrO_2 catalysts showed high NO conversion to N_2 at low temperature through a nitrous oxide (N_2O) intermediate for a NO–CO reaction. As the supporter, ZrO_2 has better performance than CeO_2 in reducing the energy barrier of NO dissociation [12]. Besides, ZrO_2 also provides abundant NO_x adsorption sites [13–15], which is beneficial for NO reduction. Koga et al. discovered that c-ZrO_2 (110) ultrathin film covering a Cu surface exhibited high NO_x reduction activity [16].

NO reduction by CO may simultaneously eliminate two kinds of pollutants and convert them into harmless CO_2 and inactive N_2, via the stoichiometric reaction $2CO + 2NO \rightarrow 2CO_2 + N_2$. Dramatically,

isocyanate (NCO) species and gas phase N_2O were detected via experimental equipment during the reaction of NO with CO [17,18]. NO–CO reaction mechanisms involving NCO and N_2O as intermediate complex have been considered on Co_3O_4 (110)-B [19], Pd/γ-Al_2O_3 (110) [20], and Cu-doped $SrTiO_3$ (100) [21] catalyst surfaces. It is widely believed that CO abstracts lattice oxygen of catalyst to produce CO_2 and oxygen vacancy through the Mars–van Krevelen mechanism [22], and then NO reduction occur on the defective catalyst surface via NCO or N_2O intermediate species to form N_2. Although previous studies have provided significant insight on NO–CO catalytic reaction mechanism, the catalytic cycle paths of NO reduction by CO on ZrO_2 surfaces remain elusive.

Surface formation energies of three low-index c-ZrO_2 (100), (110) and (111) were computed, as shown in Table S1. In this study, we adopted the most stable surface (111) and a relatively reactive surface (110) as the exposed surfaces. The adsorption behaviors of CO and NO on ZrO_2 (110) and (111) surfaces and possible reaction pathways for CO_2 and N_2 formation with corresponding energy evolution were carefully discussed based on DFT calculations. Through in-depth analysis and research, the role of reaction intermediates NCO and N_2O in catalytic reactions will be clarified, which can solve the key scientific problems and disputes existing in the current experiments.

2. Results and Discussion

2.1. CO and NO Adsorption on ZrO_2 (110) Surface

The structure models of ZrO_2 (110) surface, as shown in Figure 1a, exposes threefold coordinated O (O_{3c}) and sixfold coordinated Zr (Zr_{6c}) atoms. In the surface, the Zr–Zr bond distance is 3.710 Å and the Zr–O bond distance is 2.247 Å. The lattice constant of ZrO_2 bulk is 5.115 Å, which is in good agreement with experimental result of 5.090 Å [23].

Three adsorption sites were considered (Figure 1b): (1) the top site of Zr (Zr_T), (2) the top site of O (O_T), and (3) the bridge site between two O atoms (O_b). We have systematically calculated the adsorption energies of CO (C-end and O-end) and NO (N-end and O-end) gas molecules on ZrO_2 (110) surface, and the Table 1 lists all the value of E_{ads}.

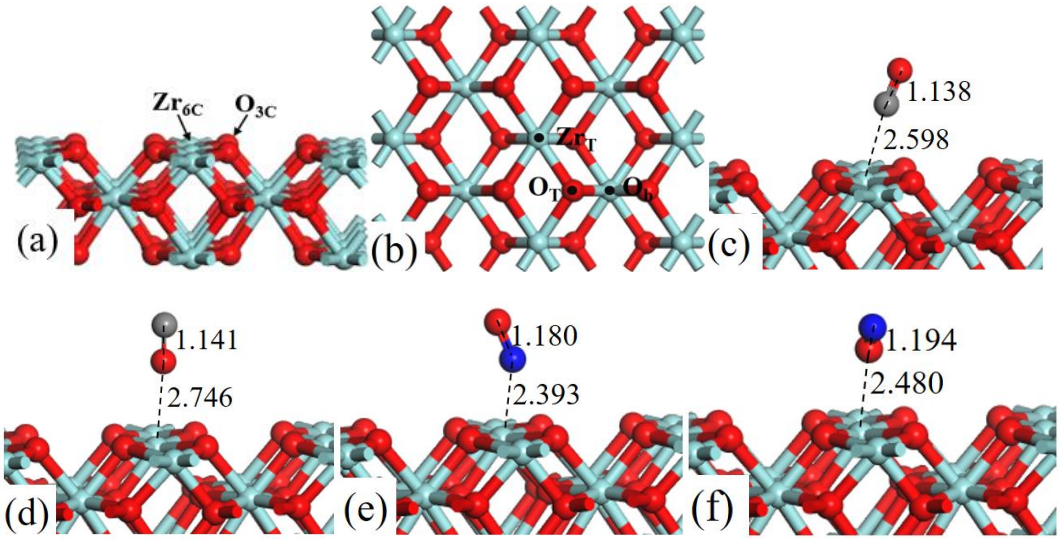

Figure 1. Structure models of (**a**) the side view and (**b**) corresponding top view of ZrO_2 (110)-2 × 2 surface. (b) Three possible adsorption sites for CO and NO gas molecules are labeled. Optimized adsorption structures of (**c**) CO C-end, (**d**) CO O-end, (**e**) NO N-end, and (**f**) NO O-end on Zr_T site. Red, cyan, gray, and blue spheres represent the O, Zr, C, and N atoms, respectively.

Table 1. Adsorption energies (E_{ads}) of CO and NO gas molecules on the different adsorption sites of ZrO_2 (110) surface.

Gas Molecule		Adsorption Site	E_{ads} (eV)	Figure
CO	C-end	Zr_T	−0.676	1(c)
		O_T	−0.675	-
		O_b	−0.227	-
	O-end	Zr_T	−0.359	1(d)
		O_T	−0.257	-
		O_b	−0.231	-
NO	N-end	Zr_T	−0.788	1(e)
		O_T	−0.776	-
		O_b	−0.253	-
	O-end	Zr_T	−0.575	1(f)
		O_T	−0.290	-
		O_b	−0.047	-

As shown in Figure 1, after fully structural optimization, CO (C-end and O-end) and NO (N-end and O-end) gas molecules preferred to adsorb on Zr_T site of ZrO_2 (110) surface. As for CO molecule adsorption, E_{ads} of CO (C-end and O-end) adsorbed on Zr_T site was −0.676 eV and −0.360 eV, respectively, indicating the C-end adsorption was more energetically favorable than O-end. In the same way NO N-end adsorption was more stable than NO O-end adsorption on ZrO_2 (110) surfaces. Coordinates for all the optimized structures were presented in Table S3.

2.2. Reaction Mechanism of NO Reduction with CO on ZrO_2 (110) Surface

2.2.1. Path 1

The Mars−van Krevelen (MvK) mechanism is a universal reaction step for CO oxidation [24] and NO–CO reaction [19] on metal oxide surfaces. As shown in Figure 2, the NO–CO catalytic cycle reaction started when the first CO gas molecule adsorbed on Zr_T site (state *ii*) with an adsorption energy of −0.676 eV, and with the change of lattice O–C distance to 3.098 Å. After adsorption, CO extracted surface oxygen atom to form CO_2 and a surface oxygen vacancy (state *iii*) through the MvK mechanism. In the corresponding transition state (TS1), the lattice O-CO bond decreased to 1.568 Å and the lattice O–C–O angle changed to 116.105°. Moreover, the energy barrier for this process was 1.948 eV, the result clearly shows that CO oxidation reaction can happen smoothly on ZrO_2 (110) surface by using exhaust temperature. We calculated two cycle reaction mechanisms (path 1 and path 2) and N_2O formation mechanism all share common steps to form oxygen vacancies on ZrO_2 (110) surface.

In the next step, CO_2 desorption into the gas phase (state *iv*) costs energy of 0.283 eV, then O_V was occupied by the first NO gas molecule forming a O_V-NO complex structure (state *v*), and the energy of 2.310 eV is released. Subsequently, the next CO weakly adsorbed to adjacent O atom of the NO (state *vi*) with an adsorption energy of −0.510 eV. In TS2, the N-O bond broke and O atom moved toward CO to form OC-O bond by overcoming an energy barrier of 2.263 eV, and the OC-O bond length was changed from 2.683 Å at state *vi* to 1.637 Å. After TS2, the second CO_2 molecule formation occurs (state *vii*). The reaction was exothermic by 1.246 eV. The similar reaction steps have been explored for Pd/γ-Al_2O_3 (110), the second CO abstracted lattice O atom from N-loaded Pd/γ-Al_2O_3 (110) surface with an energy barrier of 1.88 eV [20].

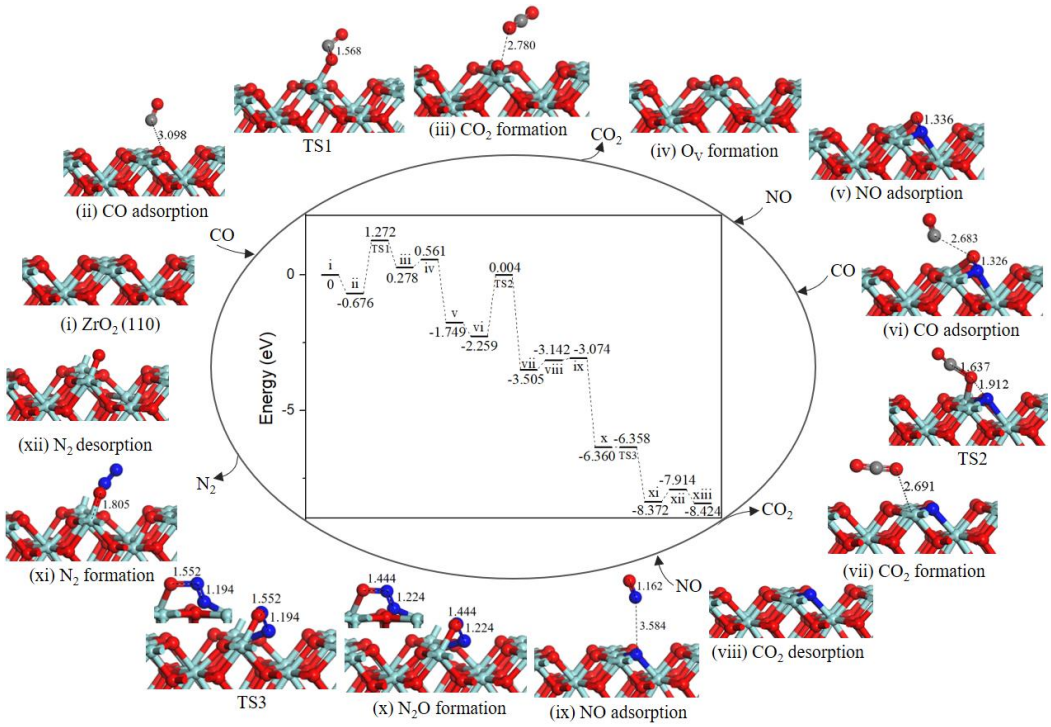

Figure 2. Energy profile and structure models of reactants, transition states and products for path 1 (NO N-end embed in oxygen vacancy site on ZrO_2 (110) surface). The energy profile is placed in the center, and structure models are placed around.

Then, the second CO_2 desorbed into the gas phase leaving a N-doped surface (state *vii*), in which N atom embedded at surface oxygen vacancy site. The desorption energy of CO_2 is approximately 0.3 eV, the interaction of ZrO_2 surface with CO_2 was much weaker than that with NO ($E_{ads} \approx 0.7$ eV), which have been reported by Luo et al. [13]. After the second CO_2 desorption, the second NO gas molecule located at N-doped ZrO_2 (110) surface (state *ix*) with the binding energy of −0.068 eV. Once NO interacted with the embedded N atom, formation of a relatively stable intermediate complex bent N_2O (state *x*) was very easy. As we can see from the energy profile (Figure 2), the process could facilely occur without energy barrier and release 3.286 eV energy. The energy barrier for N_2O dissociation was extremely low only 0.002 eV. After TS3, N-O bond and N-Zr bond dissociated to produce N_2 (state *xi*), then N_2 desorption into gas phase cost 0.458 eV, O atom successively diffused to oxygen vacancy site via an obvious barrierless process with releasing energy of 0.510 eV, the integrated ZrO_2 (110) surface was recovered eventually.

Accordingly, from calculated energy profile (Figure 2), the overall catalytic cycle is strongly exothermic. However, the second CO oxidation has greater activation energy of 2.263 eV, determining the rate of catalytic cycle. We proposed the other catalytic cycle path to produce CO_2 and N_2 via NCO species.

2.2.2. Path 2

As presented in Figure 3, the reaction mechanism of O_V surface formation is shared with path 1. Subsequently, NO adsorbed on O_V site, the value of NO O-end adsorption was −1.605 eV, which bound weaker than that of NO N-end. Then, the second CO directly combined with N atom to generate the NCO intermediate (−1.614 eV, state *vi*). The second NO adsorbed on Zr_T site adjacent to NCO complex (−0.208 eV, state *vii*). In the co-adsorption configuration, NCO and NO moved toward each other via TS2 to form a $NNCO_2$ four-membered ring intermediate (state *viii*) with an energy barrier of 0.355 eV. The subsequent step was $NNCO_2$ intermediate dissociation to produce N_2 and CO_2 (state *ix*) with a

barrier of only 0.141 eV. With N_2 and CO_2 desorption by costing 0.563 eV energy, the catalytic surface was recovered.

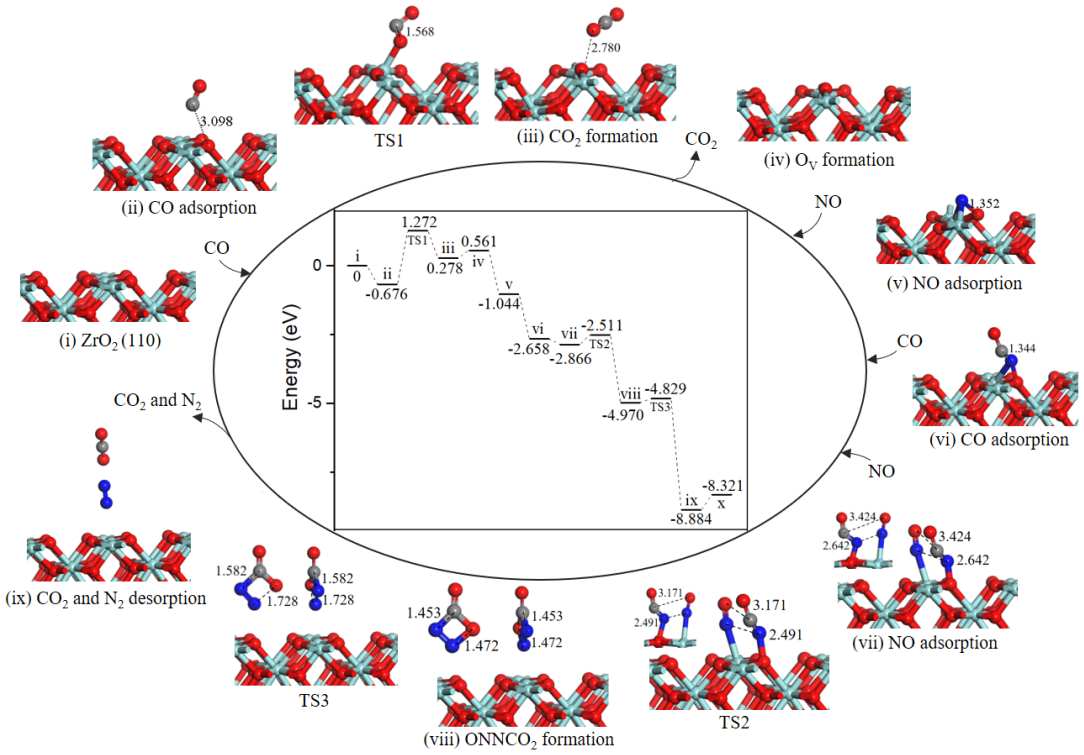

Figure 3. Energy profile and structure models of reactants, transition states and products for path 2 (NO O-end embed in oxygen vacancy site on ZrO_2 (110) surface). The energy profile is placed in the center, and structure models are placed around.

As we can see from the energy profile (Figure 3), the rate-determining step is the CO oxidation by the lattice oxygen, indicting ZrO_2 (110) surface exhibits weakly catalytic activity for low-temperature oxidation of CO. Liang et al. observed that c-ZrO_2 ultrafine powder showed relatively high activity for CO oxidation with light-off temperature at ~280 °C (50% conversion) and ~550 °C (100% conversion) [25,26]. As reported in the literature, metal doping was particularly effective for the formation of oxygen vacancy [21,27]. As for NO reduction reaction, the formation of oxygen vacancy is crucial for NO adsorption and reduction reaction [28–30]. On defective ZrO_2 (110) surface, NO decomposition and N_2 formation are occur easily as a result of a very small barrier of 0.355 eV via path 2. Although for the defective Co_3O_4 (110)-B surface [19], the most favorable NO reduction processes are energetically less competitive with a higher barrier of 1.48 eV, i.e., the ZrO_2 (110) surface is remarkable for NO reduction.

2.2.3. N_2O formation.

Beginning with the oxygen vacancy surface (state *iv*, Figure 4) the first gas NO molecule located at O_V site (state *v*, Figure 4) by releasing 1.605 eV energy, the second incoming NO molecule N-end bound with surface N atom (state *vi*, Figure 4) with strong exothermicity of 2.872 eV. Subsequently, the ONN-O bond broke into N_2O via TS2 (Figure 4). After TS2, the gas-phase N_2O (state *vii*, Figure 4) formation, the barrier for the process was 0.987 eV, the reaction was exothermic by 1.345 eV. Eventually, N_2O desorption into the gas phase (state *viii*, Figure 4) cost 0.456 eV and ZrO_2 (110) surface recovered.

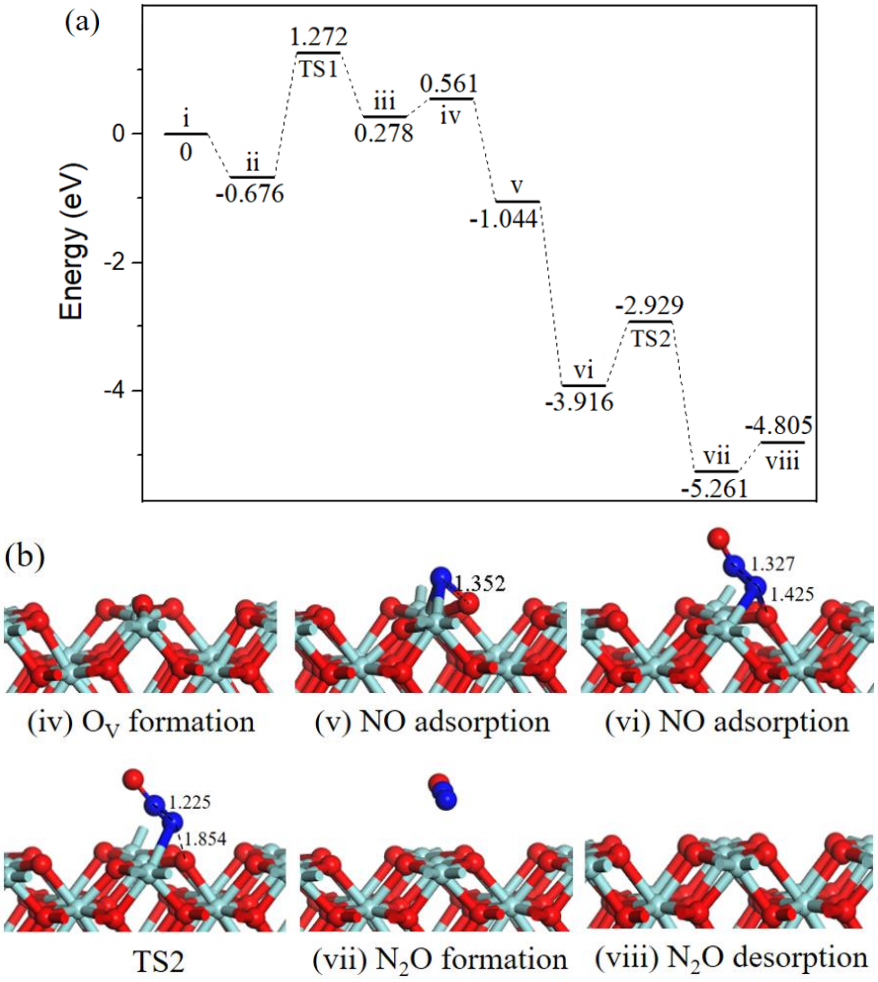

Figure 4. Energy profile (**a**) and structure models (**b**) of reactants, transition states and products for N_2O formation on ZrO_2 (110) surface. The energy profile is placed above, and structure models are placed below.

In cold start engines or lean-burn conditions N_2O is the main by-product of NO reduction [31], and the formation of N_2O on ZrO_2 surface has been observed through NO temperature-programmed desorption experiment [13]. N_2O is one of the six greenhouse gases specified in the Kyoto Protocol, the greenhouse activity is 310 times of CO_2 [32]. Catalytic systems for N_2O decomposition should be employed in catalytic converters.

Three reaction pathways have been calculated on the ZrO_2 (110) surface: the gas phase N_2O was observed via experimental equipment and in [18] it was also formed by theoretical calculation; our work provides the mechanism of N_2O formation. Path 1 involving bent N_2O intermediate was proposed to produce harmless CO_2 and inactive N_2, this cycle had a relatively high barrier than path 2 involving surface NCO intermediate, indicting CO_2 and N_2 formation mainly through path 2. Besides, the activation barriers for N_2O and N_2 formation on O_V-ZrO_2 (110) surface were 0.987 eV and 0.355 eV, respectively. The results imply that NO is selectively converted to N_2 versus N_2O under mild conditions.

2.3. CO and NO Adsorption on ZrO_2 (111) Surface

ZrO_2 (111) surface consists of 3-fold-coordinated oxygen atoms (O_{3c}) and 7-fold-coordinated zirconium atoms (Zr_{7c}), as shown in Figure 5a.

In Figure 5b three possible adsorption sites are labeled: (1) the top site of Zr (Zr_T); (2) the top site of O (O_T); (3) the 3-fold O-hollow site (O_H). The value of adsorption energies is listed in Table 2.

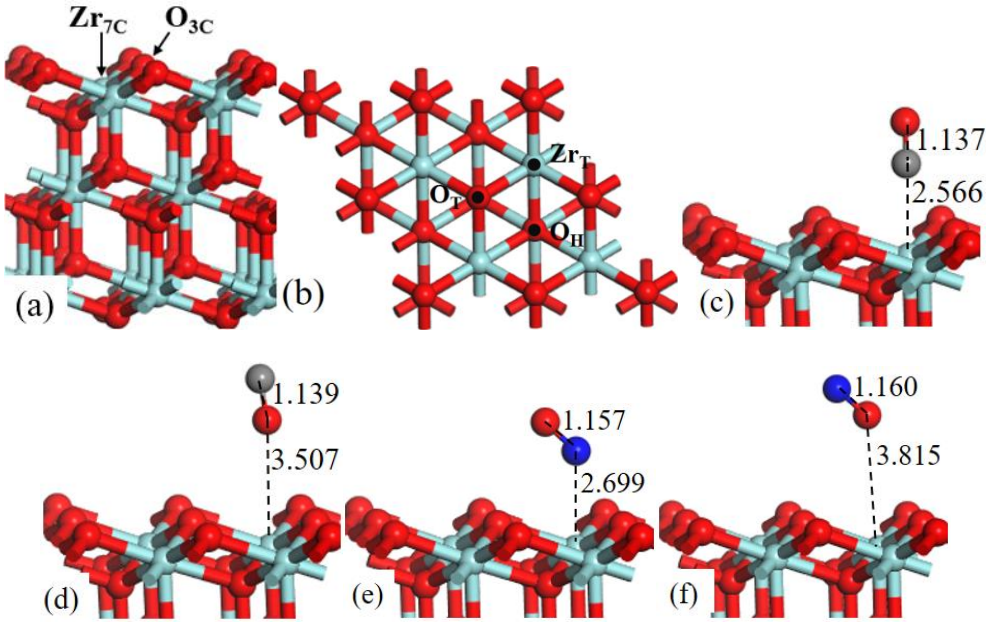

Figure 5. Structure models of (**a**) the side view and (**b**) corresponding top view of ZrO_2 (111)-2 × 2 surface. (b) Three possible adsorption sites for CO and NO gas molecules are labeled. Optimized adsorption structures of (**c**) CO C-end, (**d**) CO O-end, (**e**) NO N-end, and (**f**) NO O-end on Zr_T site.

Table 2. Adsorption energies (E_{ads}) of CO and NO gas molecules on the different adsorption sites of ZrO_2 (111) surface.

Gas Molecule		Adsorption site	E_{ads} (eV)	Figure
CO	C-end	Zr_T	−0.410	5(c)
		O_T	−0.129	-
		O_H	−0.160	-
	O-end	Zr_T	−0.162	5(d)
		O_T	−0.133	-
		O_H	−0.154	-
NO	N-end	Zr_T	−0.041	5(e)
		O_T	0.078	-
		O_H	0.046	-
	O-end	Zr_T	0.054	5(f)
		O_T	0.076	-
		O_H	0.055	-

For the adsorption behavior of CO (C-end and O-end) and NO (N-end and O-end) on ZrO_2 (111) surface, we again researched that the Zr_T site was the most favorable adsorption site; the CO C-end adsorbed on Zr_T site had maximum adsorption energy −0.788 eV, which suggested that CO C-end adsorption was slightly preferred on ZrO_2 (111) surface. Moreover, NO O-end adsorption was thermodynamically impossible, because of the positive E_{ads}.

2.4. Reaction Mechanism of NO Reduction with CO on ZrO_2 (111) Surface

2.4.1. Path 1′

Based on the lowest energy structures of CO and NO on ZrO_2 (111) surface, the first step was gas-phase CO interaction with surface Zr atom (−0.410 eV, state *ii*), as shown in Figure 6, CO may incorporate lattice O via TS1 where the distance between CO molecule and O atoms was decreased from 2.787 Å to1.246 Å. After TS1, a gas phase CO_2 molecule (state *iii*) formed. The energy barrier was equivalent to 2.949 eV. Next, CO_2 overcame 0.130 eV binding energy desorption into

gas-phase. Specifically, the following path 1′ and N_2O formation mechanisms share as common steps as discussed above.

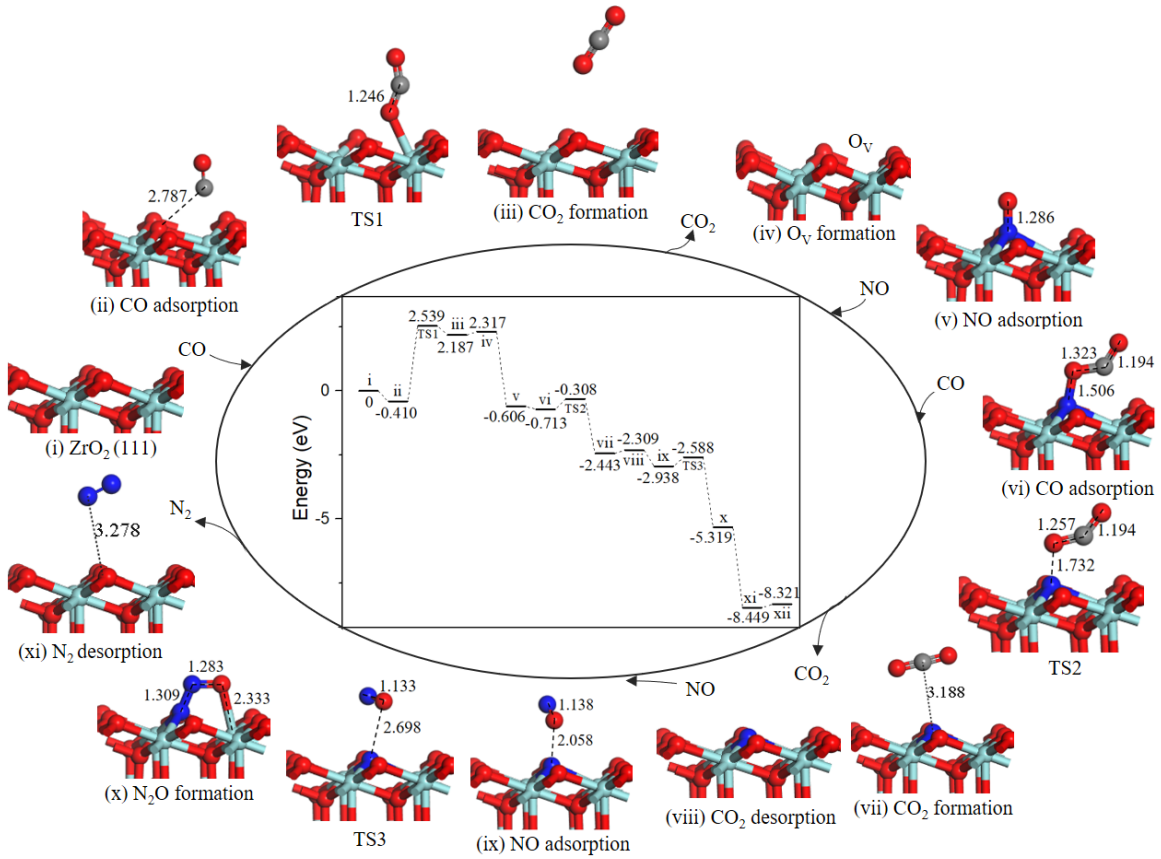

Figure 6. Energy profile and structure models of reactants, transition states and products for path 1′ (NO N-end embed in oxygen vacancy site on ZrO_2 (111) surface). The energy profile is placed in the center, and structure models are placed around.

Note that the energy barrier corresponding to TS1 (2.949 eV, Figure 6) is evidently high and oxygen vacancy formation on ZrO_2 (111) surface is difficult at low-temperature. Once oxygen vacancy formation on ZrO_2 (111) surface, NO adsorption and reduction are facile.

In state *v*, the NO molecule N-end was located at O_V site with a strong exothermicity of 2.923 eV. Subsequently, the second CO bonded with O atom of the NO to form a NOCO complex (−0.107 eV, state *vi*). The second CO_2 formation (state *vii*) arose from NOCO complex with an energy barrier of 0.405 eV (TS2). Desorption of CO_2 cost 0.134 eV. Then, the second NO adsorption on the N-doped surface (−0.629 eV, state *ix*) via TS3 forms the intermediate N_2O (state *x*) with a small barrier of 0.350 eV. Followed by a barrierless process of N_2O decomposition to generate N_2 (state *xi*). With the N_2 desorption, the surface was recovered.

2.4.2. Path 2′

As shown in Figure 7, after the formation of oxygen vacancy, the O_V site was naturally replenished by NO molecule O-end (−3.056 eV, state *v*). The second CO approached toward N atom of adsorbed NO (−0.382 eV, state *vi*) to generate the NCO intermediate (state *vii*) through TS2) and an energy barrier of 0.385 eV was needed. The next NO could adsorb close to NCO complex (−1.582 eV, state *viii*) to realize the formation of four-membered ring intermediate $NNCO_2$ (state *ix*). The activation barrier for this process was 1.194 eV. Subsequently, the N–C bond and N–O bond cleavage of four-membered

ring $NNCO_2$ led to CO_2 and N_2 formation (state *x*), with an almost barrierless processes (0.006 eV). Desorption of CO_2 and N_2 cost 0.255 eV.

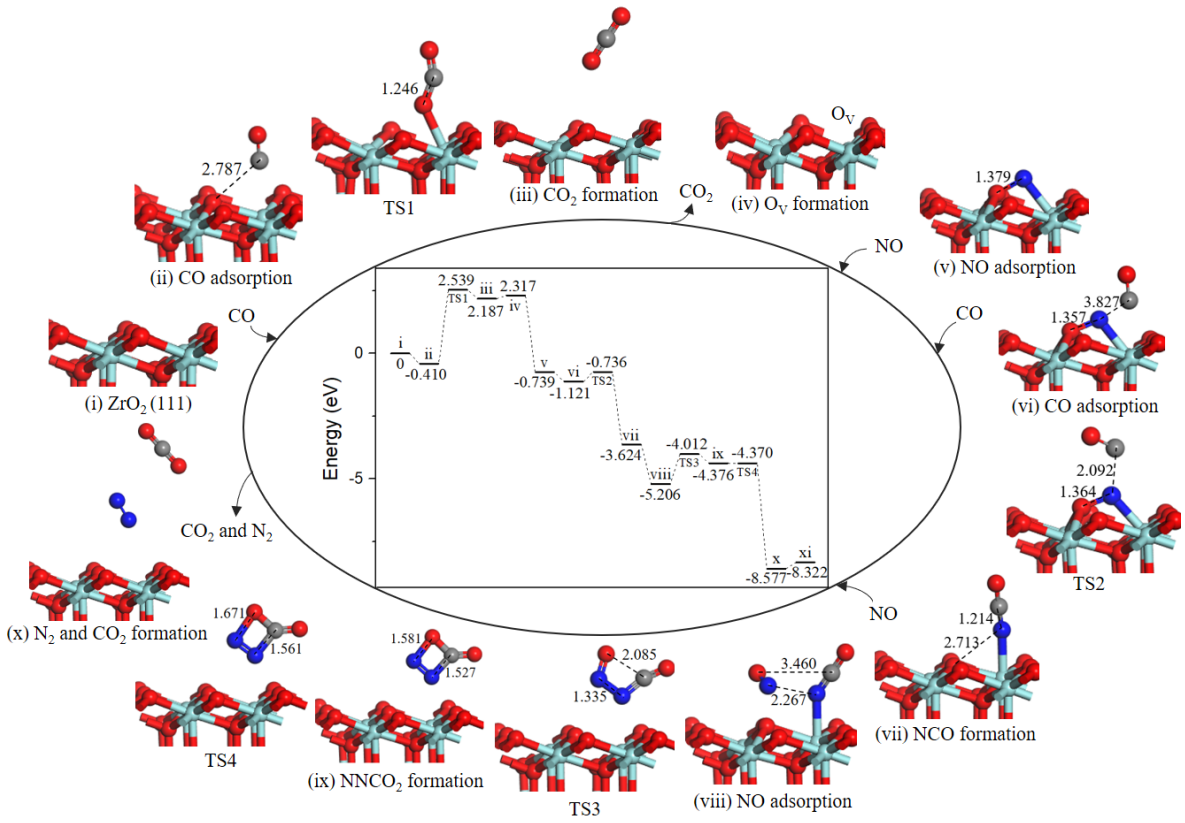

Figure 7. Energy profile and structure models of reactants, transition states and products for path 2′ (NO O-end embed in oxygen vacancy site on ZrO_2 (111) surface). The energy profile is placed in the center, and structure models are placed around.

2.4.3. Mechanism involving N_2O

The formation process of N_2O was same as the case found on ZrO_2 (110) surface. The second NO bonded with N atom of first adsorbed NO. With the N-O and N-Zr bond dissociation, N_2O formation. The energy profile and corresponding structure models of reactant, transition state and product were illustrated in Figure 8.

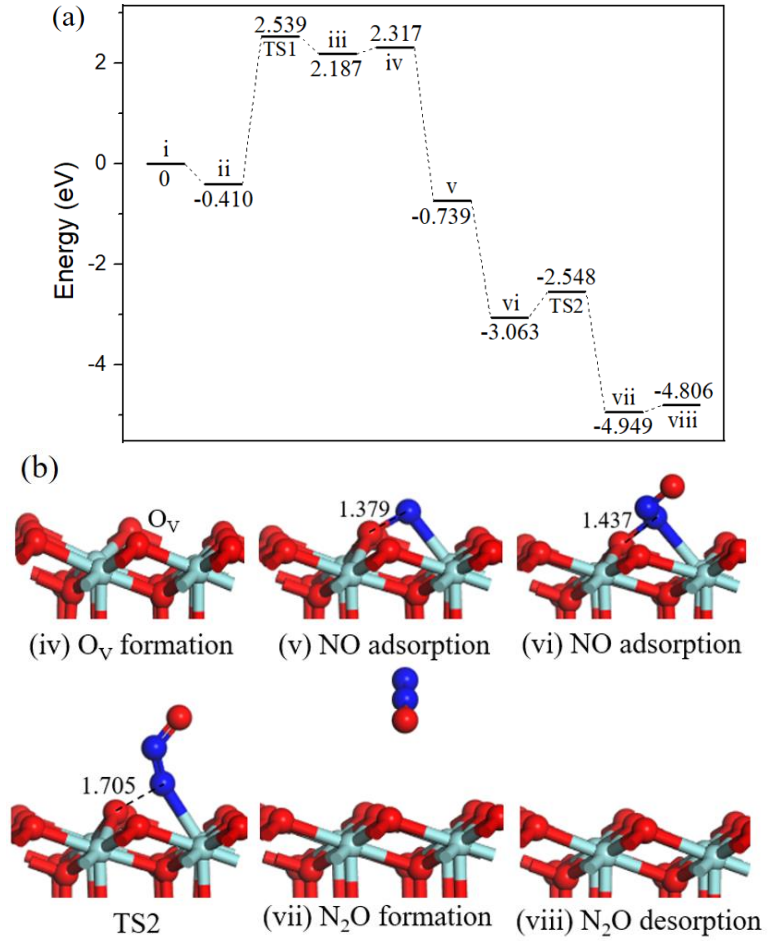

Figure 8. Energy profile (**a**) and structure models (**b**) of reactants, transition states, and products for N_2O formation on ZrO_2 (111) surface. The energy profile is placed above, and structure models are placed below.

As N_2O is a hazardous by-product, its decomposition processes have been conducted on transition metal surfaces [33,34]. Following with the decomposition mechanism of N_2O on Pd-O_V/γ-Al_2O_3 (110) surface proposed by Gao [20]. We calculated N_2O decomposition process on O_V-ZrO_2 (111) surface, as shown in Figure 9. The binding energy of N_2O adsorption was equivalent to −0.166 eV, in the corresponding transition state the N–O bond length increased from 1.195 Å to 1.288 Å. By breaking the already activated N–O bond, the desired product N_2 was formed and the dissociated O atom filled the O_V. The reaction barrier for N_2O decomposition is 0.288 eV, and the N_2 desorption from the ZrO_2 (111) surface requires 0.128 eV.

From calculated energy barriers, we found that CO oxidation by surface lattice oxygen was the rate-determining step during the process of NO reduction with CO, the reaction barriers were 1.948 eV and 2.949 eV on ZrO_2 (110) and (111) surfaces, respectively. The results indicated that compared with ZrO_2 (111) surface, ZrO_2 (110) surface had more remarkable ability to catalyze NO reduction with CO because of the lower activation barrier. From the calculated adsorption energies, CO and NO all preferred to adsorb on ZrO_2 (110) surface, which is consistent with the results of surface formation energies for (110) surface was relatively reactive than (111) surface. For the reaction mechanism of NO reduction by CO, similar reaction processes were found on ZrO_2 (110) and (111) surfaces. Intermediate complex bent N_2O was produced during path 1, path 1′ and → NCO intermediate was produced during path 2, path 2′, hazardous N_2O gas molecule was formed both on ZrO_2 (110) and (111) surfaces.

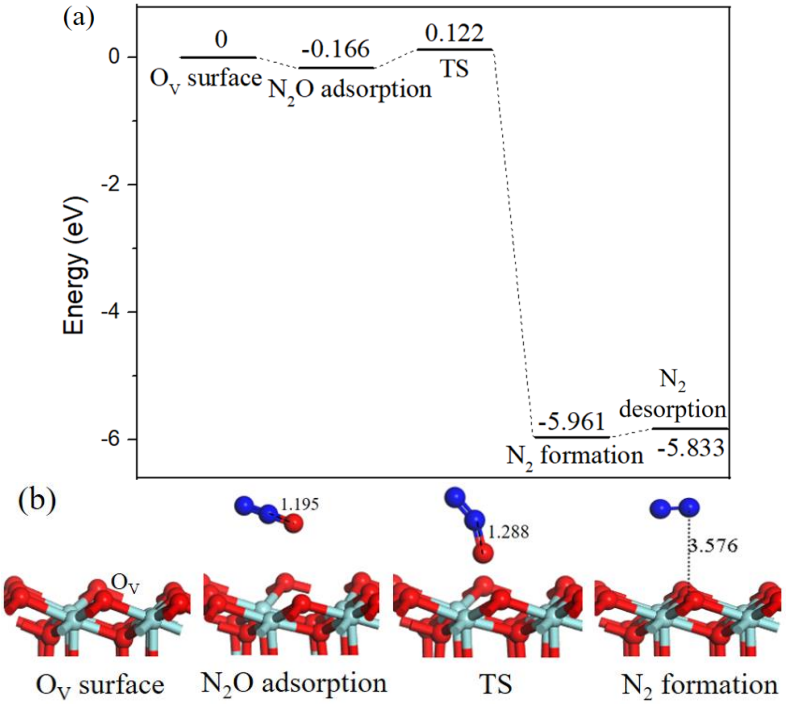

Figure 9. Energy profile (**a**) and structure models (**b**) of reactants, transition states and products for N_2O adsorb on oxygen vacancy ZrO_2 (111) surface to generate N_2 (g). The energy profile is placed above, and structure models are placed below.

3. Materials and Methods

Periodic DFT calculations were executed using DMol^3 module of Material Studio software package [35,36]. The exchange-correlation functional was treated by generalized gradient approximation with the Perdew-Wang 91 (GGA-PW91) [37]. The double numerical plus d-functions (DND) basis set was used to optimize all spin unrestricted structures. SCF tolerance was employed to 1.0×10^{-5}, the convergence tolerance of maximum energy change, maximum force, and maximum displacement were set as 2.0×10^{-5} Ha, 0.004 Ha/Å, and 0.005 Å, respectively. The transition states (TS) were calculated with linear synchronous transit (LST) and quadratic synchronous transit (QST) method [38,39] and vibrational analysis was performed to identify TS have only one imaginary frequency.

The slab models of ZrO_2 (110) and (111) surfaces were built with a 15–20 Å vacuum thickness to avoid interaction between neighboring slabs. The ZrO_2 (110) surface consisting of four atomic layers with the lowest two layers being kept fixed in their bulk positions, whereas the others were allowed to relax with adsorbed molecules. The Brillouin zone was sampled with a $(1 \times 2 \times 1)$ Monkhorst–Pack k-point grid [40]. The ZrO_2 (111) surface consisting of six atomic layers with the bottom four layers were kept fixed and the top two layers were relaxed. A $(2 \times 2 \times 1)$ Monkost–Pack grid [40] for the ZrO_2 (111) surface geometry optimization. In all cases, an orbital cutoff of 5.0 Å was used to improve the computational performance and a 2×2 supercell was applied.

The adsorption energies (E_{ads}) of CO and NO gas molecules on ZrO_2 (110) and (111) surfaces were calculated by the following formula,

$$E_{ads} = E_{(surface + gas\ molecules)} - E_{(surface)} - E_{(gas\ molecules)} \quad (1)$$

where $E_{(surface + gas\ molecules)}$ is the total energy of the system involving the ZrO_2 (110) or (111) catalyst with the adsorbed CO or NO gas molecule, $E_{(surface)}$ is the total energy of isolated ZrO_2 (110) or (111) surface, and $E_{(gas\ molecules)}$ is the total energy of a single CO or NO gas molecule.

To validate the methods, we calculated the energy of NO, CO, N_2 and CO_2 molecules in a large unit cell of 10 Å × 10 Å × 10 Å, and compared the bond distances with the values calculated at the B3LYP/6-31G(d) level [41]. We listed all the values in Table S2, the calculated bond distances were within 1% of ones.

4. Conclusions

In summary, DFT calculations were performed to investigate NO reduction with CO on ZrO_2 (110) and (111) surfaces. For the ZrO_2 (110) surface, two cycle reaction pathways (paths 1 and 2) for CO_2 and N_2 formation were presented, and the path 2 involving the process of the NCO intermediate interaction with NO was energetically favorable. The similar cycle reaction pathways (paths 1′ and 2′) were found on ZrO_2 (111) surface, but CO oxidation by lattice O had a significantly higher energy barrier of 2.949 eV. The results indicated that compared with ZrO_2 (111) surface, ZrO_2 (110) surface had more remarkable ability to catalyze NO reduction with CO. Our calculations also clearly showed that the existence of oxygen vacancies on ZrO_2 (110) and (111) surfaces were crucial for NO adsorption and reduction reaction. NO healing O_V was a strongly exothermic process (2.0–3.0 eV) and successive reactions all exhibited lower energy barriers, especially path 2 (0.355 eV) and path 1′ (0.405eV). The mechanism involving N_2O also was explored, and the activation barriers for N_2O formation on O_V-ZrO_2 (110) and (111) were 0.987 eV and 0.515 eV, respectively. The relatively higher barriers imply that NO is selectively converted to N_2 versus N_2O under mild conditions.

Supplementary Materials: Supplementary materials can be found at http://www.mdpi.com/1422-0067/20/24/6129/s1.

Author Contributions: Conceptualization, C.Z. and X.S.; methodology, X.C. and Z.W.; software, X.C. and Z.W.; validation, X.S.; formal analysis, X.C. and Z.W.; investigation, C.Z. and X.S.; resources, X.S.; data curation, X.C.; writing—original draft preparation, X.C.; writing—review and editing, C.Z. and X.S.; supervision, X.S.; project administration, C.Z. and X.S.; funding acquisition, C.Z. and X.S.

Funding: This research was funded by the National Natural Science Foundation of China (21607011, 21976109), the Key Research and Development Project of Shandong Province (2019GSF109021, 2019GSF109037), the Natural Science Foundation of Shandong Province (ZR2018MB043), and the Fundamental Research Funds of Shandong University (2018JC027).

Conflicts of Interest: The authors declare no conflicts of interest.

References

1. Taylor, K.C. Nitric Oxide Catalysis in Automotive Exhaust Systems. *Catal. Rev.* **1993**, *35*, 457–481. [CrossRef]
2. Shelef, M.; Graham, G.W. Why Rhodium in Automotive Three-Way Catalysts? *Catal. Rev.* **1994**, *36*, 433–457. [CrossRef]
3. Lin, J.; Ma, C.; Wang, Q.; Xu, Y.; Ma, G.; Wang, J.; Wang, H.; Dong, C.; Zhang, C.; Ding, M. Enhanced low-temperature performance of CO_2 methanation over mesoporous Ni/Al_2O_3-ZrO_2 catalysts. *Appl. Catal. B Environ.* **2019**, *243*, 262–272. [CrossRef]
4. Romero-Sáez, M.; Dongil, A.B.; Benito, N.; Espinoza-González, R.; Escalona, N.; Gracia, F. CO_2 methanation over nickel-ZrO_2 catalyst supported on carbon nanotubes: A comparison between two impregnation strategies. *Appl. Catal. B Environ.* **2018**, *237*, 817–825. [CrossRef]
5. Chen, C.; Ruan, C.; Zhan, Y.; Lin, X.; Zheng, Q.; Wei, K. The significant role of oxygen vacancy in Cu/ZrO_2 catalyst for enhancing water-gas-shift performance. *Int. J. Hydrog. Energy* **2014**, *39*, 317–324. [CrossRef]
6. Kauppinen, M.M.; Melander, M.M.; Bazhenov, A.S.; Honkala, K. Unraveling the Role of the Rh–ZrO_2 Interface in the Water-Gas-Shift Reaction via a First-Principles Microkinetic Study. *ACS Catal.* **2018**, *8*, 11633–11647. [CrossRef]
7. Yao, X.; Chen, L.; Cao, J.; Chen, Y.; Tian, M.; Yang, F.; Sun, J.; Tang, C.; Dong, L. Enhancing the *de*NO_x performance of MnO_x/CeO_2-ZrO_2 nanorod catalyst for low-temperature NH_3-SCR by TiO_2 modification. *Chem. Eng. J.* **2019**, *369*, 46–56. [CrossRef]

8. Liu, S.; Wang, H.; Wei, Y.; Zhang, R.; Royer, S. Morphology-Oriented ZrO_2-Supported Vanadium Oxide for the NH_3-SCR Process: Importance of Structural and Textural Properties. *ACS Appl. Mater. Interfaces* **2019**, *11*, 22240–22254. [CrossRef]
9. De Souza, P.M.; Rabelo-Neto, R.C.; Borges, L.E.P.; Jacobs, G.; Davis, B.H.; Graham, U.M.; Resasco, D.E.; Noronha, F.B. Effect of Zirconia Morphology on Hydrodeoxygenation of Phenol over Pd/ZrO_2. *ACS Catal.* **2015**, *5*, 7385–7398. [CrossRef]
10. Ohta, H.; Feng, B.; Kobayashi, H.; Hara, K.; Fukuoka, A. Selective hydrodeoxygenation of lignin-related 4-propylphenol into n-propylbenzene in water by Pt-Re/ZrO_2 catalysts. *Catal. Today* **2014**, *234*, 139–144. [CrossRef]
11. Okamoto, Y.; Gotoh, H. Copper-zirconia catalysts for NO□CO reactions. *Catal. Today* **1997**, *36*, 71–79. [CrossRef]
12. Koga, H.; Hayashi, A.; Ato, Y.; Tada, K.; Hosokawa, S.; Tanaka, T.; Okumura, M. Effect of ceria and zirconia supports on NO reduction over platinum-group metal catalysts: A DFT study with comparative experiments. *Catal. Today* **2019**, *332*, 236–244. [CrossRef]
13. Luo, M.F.; Zhong, Y.J.; Zhu, B.; Yuan, X.X.; Zheng, X.M. Temperature-programmed desorption study of NO and CO_2 over CeO_2 and ZrO_2. *Appl. Surf. Sci.* **1997**, *115*, 185–189. [CrossRef]
14. Sun, C.; Zhu, J.; Lv, Y.; Qi, L.; Liu, B.; Gao, F.; Sun, K.; Dong, L.; Chen, Y. Dispersion, reduction and catalytic performance of CuO supported on ZrO_2-doped TiO_2 for NO removal by CO. *Appl. Catal. B Environ.* **2011**, *103*, 206–220. [CrossRef]
15. Zhao, B.; Ran, R.; Wu, X.; Weng, D.; Wu, X.; Huang, C. Comparative study of Mn/TiO_2 and Mn/ZrO_2 catalysts for NO oxidation. *Catal. Commun.* **2014**, *56*, 36–40. [CrossRef]
16. Koga, H.; Tada, K.; Hayashi, A.; Ato, Y.; Okumura, M. High NO_x Reduction Activity of an Ultrathin Zirconia Film Covering a Cu Surface: A DFT Study. *Catal. Lett.* **2017**, *147*, 1827–1833. [CrossRef]
17. Kantcheva, M.; Samarskaya, O.; Ilieva, L.; Pantaleo, G.; Venezia, A.M.; Andreeva, D. In situ FT-IR investigation of the reduction of NO with CO over Au/CeO_2-Al_2O_3 catalyst in the presence and absence of H_2. *Appl. Catal. B Environ.* **2009**, *88*, 113–126. [CrossRef]
18. Sica, A.M.; Gigola, C.E. Interaction of CO, NO and NO/CO over Pd/γ-Al_2O_3 and Pd-WO_x/γ-Al_2O_3 catalysts. *Appl. Catal. A Gen.* **2003**, *239*, 121–139. [CrossRef]
19. Jin, X.; Huai, L.-Y.; Wen, H.; Yi, W.-C.; Liu, J.-Y. Reduction of NO with CO on the Co_3O_4(110)-B and CoO(110) Surfaces: A First-Principles Study. *J. Phys. Chem. C* **2019**, *123*, 1770–1778. [CrossRef]
20. Gao, H. Theoretical analysis of CO+NO reaction mechanism on the single Pd atom embedded in γ-Al_2O_3 (110) surface. *Appl. Catal. A Gen.* **2017**, *529*, 156–166. [CrossRef]
21. Carlotto, S.; Natile, M.M.; Glisenti, A.; Vittadini, A. Catalytic Mechanisms of NO Reduction in a CO–NO Atmosphere at Co- and Cu-Doped SrTiO3(100) Surfaces. *J. Phys. Chem. C* **2018**, *122*, 449–454. [CrossRef]
22. Mars, P.; van Krevelen, D.W. Oxidations carried out by means of vanadium oxide catalysts. *Chem. Eng. Sci.* **1954**, *3*, 41–59. [CrossRef]
23. Howard, C.J.; Hill, R.J.; Reichert, B.E. Structures of ZrO_2 polymorphs at room temperature by high-resolution neutron powder diffraction. *Acta Crystallogr. Sect. B* **1988**, *44*, 116–120. [CrossRef]
24. Song, W.; Hensen, E.J.M. A computational DFT study of CO oxidation on a Au nanorod supported on CeO_2(110): On the role of the support termination. *Catal. Sci. Technol.* **2013**, *3*, 3020–3029. [CrossRef]
25. Liang, L.; Dang, S.; Gao, Y. Preparation of cubic ZrO_2 ultrafine powders and characterization of their catalytic properties for CO total oxidation. *J. Fudan Univ. Nat. Sci.* **2003**, 266–269. (In Chinese) [CrossRef]
26. Liang, L.; Dang, S.; Gao, Y. Preparation of cubic ZrO_2 ultrafine powders and characterization of their catalytic properties for CO complete oxidation. *Acta Pet. Sin. Pet. Process. Sect.* **2003**, 70–75. (In Chinese)
27. Carlotto, S.; Natile, M.M.; Glisenti, A.; Paul, J.-F.; Blanck, D.; Vittadini, A. Energetics of CO oxidation on lanthanide-free perovskite systems: The case of Co-doped $SrTiO_3$. *Phys. Chem. Chem. Phys.* **2016**, *18*, 33282–33286. [CrossRef]
28. Azad, S.; Szanyi, J.; Peden, C.H.F.; Wang, L.Q. Adsorption and reaction of NO on oxidized and reduced SrTiO3(100) surfaces. *J. Vac. Sci. Technol. A* **2003**, *21*, 1307–1311. [CrossRef]
29. Rodriguez, J.A.; Azad, S.; Wang, L.Q.; García, J.; Etxeberria, A.; González, L. Electronic and chemical properties of mixed-metal oxides: Adsorption and reaction of NO on $SrTiO_3$(100). *J. Chem. Phys.* **2003**, *118*, 6562–6571. [CrossRef]

30. Zhu, J.; Xiao, D.; Li, J.; Yang, X.; Wu, Y. Mechanism of NO decomposition on perovskite (-like) catalysts. *Chin. Sci. Bull.* **2005**, *50*, 707–710. [CrossRef]
31. Fritz, A.; Pitchon, V. The current state of research on automotive lean NO_x catalysis. *Appl. Catal. B Environ.* **1997**, *13*, 1–25. [CrossRef]
32. Liu, J.; Wang, L.; Song, W.; Zhao, M.; Liu, J.; Wang, H.; Zhao, Z.; Xu, C.; Duan, Z. $BiMO_x$ Semiconductors as Catalysts for Photocatalytic Decomposition of N2O: A Combination of Experimental and DFT+U Study. *ACS Sustain. Chem. Eng.* **2019**, *7*, 2811–2820. [CrossRef]
33. Tan, L.; Huang, L.; Liu, Y.; Wang, Q. Detailed mechanism of the NO+CO reaction on Rh(100) and Rh(111): A first-principles study. *Appl. Surf. Sci.* **2018**, *444*, 276–286. [CrossRef]
34. Zhang, J.; Gong, X.; Lu, G. DFT + U study of the CO + NO_x reaction on a CeO_2(110)-supported Au nanoparticle. *Chin. J. Catal.* **2014**, *35*, 1305–1317. [CrossRef]
35. Delley, B. An all-electron numerical method for solving the local density functional for polyatomic molecules. *J. Chem. Phys.* **1990**, *92*, 508–517. [CrossRef]
36. Delley, B. From molecules to solids with the $DMol_3$ approach. *J. Chem. Phys.* **2000**, *113*, 7756–7764. [CrossRef]
37. Perdew, J.P.; Wang, Y. Accurate and simple analytic representation of the electron-gas correlation energy. *Phys. Rev. B* **1992**, *45*, 13244–13249. [CrossRef]
38. Elber, R.; Karplus, M. A method for determining reaction paths in large molecules: Application to myoglobin. *Chem. Phys. Lett.* **1987**, *139*, 375–380. [CrossRef]
39. Halgren, T.A.; Lipscomb, W.N. The synchronous-transit method for determining reaction pathways and locating molecular transition states. *Chem. Phys. Lett.* **1977**, *49*, 225–232. [CrossRef]
40. Monkhorst, H.J.; Pack, J.D. Special points for Brillouin-zone integrations. *Phys. Rev. B* **1976**, *13*, 5188–5192. [CrossRef]
41. Irikura, K.K. Systematic Errors in ab Initio Bond Dissociation Energies. *J. Phys. Chem. A* **1998**, *102*, 9031–9039. [CrossRef]

© 2019 by the authors. Licensee MDPI, Basel, Switzerland. This article is an open access article distributed under the terms and conditions of the Creative Commons Attribution (CC BY) license (http://creativecommons.org/licenses/by/4.0/).